Effect of geometry on the classical entanglement in a chaotic optical fiber

Sijo K. Joseph,[1,*] **Juan Sabuco,**[1] **Lock Yue Chew,**[2] **and Miguel A. F. Sanjuán**[1]

[1]*Nonlinear Dynamics, Chaos and Complex Systems Group, Departamento de Física, Universidad Rey Juan Carlos, Tulipán s/n, 28933 Móstoles, Madrid, Spain*
[2]*Division of Physics and Applied Physics, School of Physical and Mathematical Sciences, Nanyang Technological University, 21 Nanyang Link, Singapore 637371, Singapore*

[*]*sijo.joseph@urjc.es*

Abstract: The effect of boundary deformation on the classical entanglement which appears in the classical electromagnetic field is considered. A chaotic billiard geometry is used to explore the influence of the mechanical modification of the optical fiber cross-sectional geometry on the production of classical entanglement within the electromagnetic fields. For the experimental realization of our idea, we propose an optical fiber with a cross section that belongs to the family of Robnik chaotic billiards. Our results show that a modification of the fiber geometry from a regular to a chaotic regime can enhance the transverse mode classical entanglement.

References and links

1. S. Chaudhury, A. Smith, B. E. Anderson, S. Ghose, and P. S. Jessen, "Quantum signs of chaos in a kicked top," Nature **461**, 768–771 (2009).
2. S. Ghose and B. C. Sanders, "Entanglement dynamics in chaotic systems," Phys. Rev. A **70**, 062315 (2004).
3. X. Wang, S. Ghose, B. C. Sanders, and B. Hu, "Entanglement as a signature of quantum chaos," Phys. Rev. E **70**, 016217 (2004).
4. S. K. Joseph, L. Y. Chew, and M. A. F. Sanjuán, "Impact of quantum-classical correspondence on entanglement enhancement by single-mode squeezing," Phys. Lett. A **378**, 2603–2610 (2014).
5. R. Gilmore and M. Lefranc, *The Topology of Chaos: Alice in Stretch and Squeezeland*, (John Wiley & Sons. Inc., 2002).
6. M. Robnik, "Classical dynamics of a family of billiards with analytic boundaries," J. Phys. A: Math. Gen. **16**, 3971 (1983).
7. L. Bunimovich, "On the ergodic properties of nowhere dispersing billiards," Commun. Math. Phys. **65**, 295–312 (1979).
8. J. N. Bandyopadhyay and A. Lakshminarayan, "Testing statistical bounds on entanglement using quantum chaos," Phys. Rev. Lett. **89**, 060402 (2002).
9. J. N. Bandyopadhyay and A. Lakshminarayan, "Entanglement production in coupled chaotic systems: Case of the kicked tops," Phys. Rev. E **69**, 016201 (2004).
10. P. A. Miller and S. Sarkar, "Signatures of chaos in the entanglement of two coupled quantum kicked tops," Phys. Rev. E **60**, 1542–1550 (1999).
11. H. Fujisaki, T. Miyadera, and A. Tanaka, "Dynamical aspects of quantum entanglement for weakly coupled kicked tops," Phys. Rev. E **67**, 066201 (2003).
12. M. Lombardi and A. Matzkin, "Entanglement and chaos in the kicked top," Phys. Rev. E **83**, 016207 (2011).
13. A. Lakshminarayan, "Entangling power of quantized chaotic systems," Phys. Rev. E **64**, 036207 (2001).
14. S.-H. Zhang and Q.-L. Jie, "Quantum-classical correspondence in entanglement production: Entropy and classical tori," Phys. Rev. A **77**, 012312 (2008).

15. N. N. Chung and L. Y. Chew, "Dependence of entanglement dynamics on the global classical dynamical regime," Phys. Rev. E **80**, 016204 (2009).
16. G. B. Lemos, R. M. Gomes, S. P. Walborn, P. H. Souto Ribeiro, and F. Toscano, "Experimental observation of quantum chaos in a beam of light," Nat. Commun. **3**, 1211 (2012).
17. A. Aiello, F. Töppel, C. Marquardt, E. Giacobino and G. Leuchs, "Quantum-like nonseparable structures in optical beams," New J. Phys. **17**, 043024 (2015).
18. V. S. Manu and A. Kumar, "Quantum simulation using fidelity-profile optimization," Phys. Rev. A **89**, 052331 (2014).
19. S. Lloyd and S. L. Braunstein, "Quantum computation over continuous variables," Phys. Rev. Lett. **82**, 1784–1787 (1999).
20. A. Rai, S. Das, and G. Agarwal, "Quantum entanglement in coupled lossy waveguides", Opt. Express **18**, 6241–6254 (2010).
21. B. N. Simon, S. Simon, F. Gori, M. Santarsiero, R. Borghi, N. Mukunda, and R. Simon, "Nonquantum entanglement resolves a basic issue in polarization optics," Phys. Rev. Lett. **104**, 023901 (2010).
22. R. J. C. Spreeuw, "A classical analogy of entanglement," Found. Phys. **28**, 361–374 (1998).
23. R. J. C. Spreeuw, "Classical wave-optics analogy of quantum-information processing," Phys. Rev. A **63**, 062302 (2001).
24. T. W. Hijmans, T. N. Huussen and R. J. C. Spreeuw, "Time and frequency domain solutions in an optical analogue of Grovers search algorithm," J. Opt. Soc. Am. B **24**, 214–220 (2007).
25. A. N. de Oliveira, S. P. Walborn and C. H. Monken, "Implementing the Deutsch algorithm with polarization and transverse spatial modes," J. Opt. B: Quantum Semiclass. Opt. **7**, 288–292 (2005).
26. B. Perez-Garcia, J. Francis, M. McLaren, R. I. Hernandez-Aranda, A. Forbes, T. Konrad, "Quantum computation with classical light: The Deutsch Algorithm," Phys. Lett. A **379**, 1675–1680 (2015).
27. A. Aiello, F. Töppel, C. Marquardt, E. Giacobino, G. Leuchs, "Classical entanglement: oxymoron or resource?" http://arxiv.org/abs/1409.0213 (2014).
28. C. T. Samlan, N. K. Viswanathan, "Quantifying classical entanglement using polarimetry: spatially-inhomogeneously polarized beams," http://arxiv.org/abs/1506.07112 (2015).
29. S. Berg-Johansen, F. Töppel, B. Stiller, P. Banzer, M. Ornigotti, E. Giacobino, G. Leuchs, A. Aiello, and C. Marquardt, "Classically entangled optical beams for high-speed kinematic sensing," Optica **2**, 864–868 (2015).
30. S. Hiroyuki and O. Megumi, "Transverse-mode beam splitter of a light beam and its application to quantum cryptography," Phys. Rev. A **68**, 012323 (2003).
31. P. Ghose and M. K. Samal, "EPR type nonlocality in classical electrodynamics," http://arxiv.org/abs/quant-ph/0111119 (2001).
32. P. Ghose and Mukhrjee, "Entanglement in classical optics," Rev. Theor. Sci. **2**, 274–288 (2014).
33. A. K. Rajagopal and P. Ghose, "Hilbert space theory of classical electrodynamics," http://arxiv.org/abs/1409.5874 (2014).
34. Y. Sun, X. Song, H. Qin, X. Zhang, Z. Yang, and X. Zhang, "Non-local classical optical correlation and implementing analogy of quantum teleportation," Sci. Rep. **5**, 9175 (2015).
35. X.-F. Qian, B. Little, J. C. Howell, and J. H. Eberly, "Shifting the quantum-classical boundary: theory and experiment for statistically classical optical fields," Optica **2**, 611–615 (2015).
36. M. A. Man'ko, V. I. Man'ko, and R. V. Mendes, "Quantum computation by quantumlike systems," Phys. Lett. A **288**, 132 (2001).
37. R. Fedele and M. A. Man'ko, "Beam optics applications: quantumlike versus classical-like domains," Eur. Phys. J. D **27**, 263 (2003).
38. M. A. Man'ko, "Analogs of time-dependent quantum phenomena in optical fibers," J. Phys.: Conf. Series **99**, 012012 (2008).
39. J. Fu, Z. Si, S. Tang, and J. Deng, "Analogs of time-dependent quantum phenomena in optical fibers," Phys. Rev. A **71**, 059901 (2005).
40. H.-J. Stöckmann and J. Stein, "Quantum chaos in billiards studied by microwave absorption," Phys. Rev. Lett. **64**, 2215–2218 (1990).
41. F. Haake, G. Lenz, P. Seba, J. Stein, H.-J. Stöckmann, and K. Życzkowski, "Manifestation of wave chaos in pseudointegrable microwave resonators," Phys. Rev. A **44**, R6161–R6164 (1991).
42. J. Stein and H.-J. Stöckmann, "Experimental determination of billiard wave functions," Phys. Rev. Lett. **68**, 2867–2870 (1992).
43. H. J. Stöckmann, *Quantum Chaos An Introduction*, (Cambridge University Press, 2000).
44. V. Doya, O. Legrand, F. Mortessagne, and C. Miniatura, "Speckle statistics in a chaotic multimode fiber," Phys. Rev. E **65**, 056223 (2002).
45. V. Doya, O. Legrand, C. Michel, and F. Mortessagne, "Optical scar in a chaotic fiber," Eur. Phys. J. Special Topics **145**, 49–61 (2007).
46. S. Chávez-Cerda, J. R. Moya-Cessa, and H. M. Moya-Cessa, "Quantumlike systems in classical optics: applications of quantum optical methods," J. Opt. Soc. Am. B **24**, 404–407 (2007).
47. S. Chávez-Cerda, H. M. M. Cessa, and J. R. M. Cessa, "Quantum-like entanglement in classical optics," Opt.

Photon. News **18**, 38 (2007).

48. K. F. Lee and J. E. Thomas, "Experimental simulation of two-particle quantum entanglement using classical fields," Phys. Rev. Lett. **88**, 097902 (2002).
49. D. D. Holm and G. Kovačič, "Homoclinic chaos for ray optics in a fiber," Physica D **51**, 177–188 (1991).
50. L. Carretero, P. Acebal, S. Blaya, C. García, A. Fimia, R. Madrigal and A. Murciano, "Nonparaxial diffraction analysis of Airy and SAiry beams", Opt. Express, **25**, 22432–22441(2009).
51. B. Nguyen and D. Grebenkov, "Localization of laplacian eigenfunctions in circular, spherical, and elliptical domains," SIAM J. Appl. Math. **73**, 780–803 (2013).
52. T. Betcke and L. Trefethen, "Reviving the method of particular solutions," SIAM Rev. **47**, 469–491 (2005).
53. T. Betcke, "The generalized singular value decomposition and the method of particular solutions," SIAM J. Sci. Comput. **30**, 1278–1295 (2008).
54. S. Parker, S. Bose, and M. B. Plenio, "Entanglement quantification and purification in continuous-variable systems," Phys. Rev. A **61**, 032305 (2000).
55. A. Bogdanov, Y. Bogdanov, and K. Valiev, "Schmidt modes and entanglement in continuous-variable quantum systems," Russ. Microelectron. **35**, 7–20 (2006).
56. J. N. Hollenhorst, "Quantum limits on resonant-mass gravitational-radiation detectors," Phys. Rev. D **19**, 1669–1679 (1979).
57. J. Rai and C. L. Mehta, "Coordinate representation of squeezed states," Phys. Rev. A **37**, 4497–4499 (1988).
58. C. M. Caves, "Quantum-mechanical noise in an interferometer," Phys. Rev. D **23**, 1693–1708 (1981).
59. K. B. Møller, T. G. Jørgensen, and J. P. Dahl, "Displaced squeezed number states: Position space representation, inner product, and some applications," Phys. Rev. A **54**, 5378–5385 (1996).
60. S. K. Joseph, L. Y. Chew, and M. A. F. Sanjuán, "Effect of squeezing and planck constant dependence in short time semiclassical entanglement," Eur. Phys. J. D **68**, 238 (2014).

1. Introduction

Recent research in quantum chaos has uncovered the relationship between chaos and entanglement both theoretically and experimentally [1–4]. It is well known that classically chaotic trajectories exhibit rich topological structures in the classical phase space [5]. Recently, there has been an increasing interest in relating quantum entanglement and classical geometry. In this article, we explore how the classical entanglement in an electromagnetic field can be intimately connected to the geometry of the domain boundary within which the fields are confined. In this context, we use the analogy between a quantum chaotic billiard in the non-relativistic quantum regime to the electromagnetic wave propagation in a chaotic optical fiber. The effects of spatial geometry on classical entanglement and its connection to Hamiltonian chaos to be an as yet unexplored direction.

Classical chaos has been observed in very simple systems like the Robnik billiard [6] and the Bunimovich stadium [7]. It is already known that a quantum system in a classically chaotic regime can generate higher entanglement [1, 8–15]. In terms of its implementation, a recent experiment has demonstrated the presence of quantum chaos in light beams [16]. While quantum entanglement has been practically implemented in sophisticated discrete-variable systems such as an NMR based system [18], there is a recent interest in the application of continuous variable entanglement for the purpose of quantum computation [19]. G. Agarwal et. al had analyzed the entanglement dynamics of coupled single mode waveguides and they have shown that the coupled waveguides can make basic units of quantum circuits [20]. Here, we follow the approach based on the analogies between quantum physics and optics via the classical electromagnetic waves [21]. It was Spreeuw who realized the existence of classical entanglement [22, 23]. Further research on this area revealed that classical entanglement can indeed be used as a resource [24–27]. In Refs. [24–26], it was shown that the Grover and Deutsch algorithms can be implemented using classical entanglement and the cryptographic application was also pointed out in Ref. [30]. Very recently, it has been shown that the classically entangled light beam can also be used for high-speed kinematic sensing [29]. In a recent experiment, researchers also found a way to quantify the classical entanglement using polarimetric measurements [28].

According to P. Ghose et al., the EPR like correlation can also appear in classical electrody-

namics [31,32]. It has been shown recently that the classical electrodynamics contains a Hilbert space structure which makes it similar to quantum mechanics in certain aspects [33]. In addition to that, in recent experiments, researchers have explored the non-quantum entanglement (classical entanglement) in the classical optical field [34, 35]. It is well known that the Maxwell's equations of the transverse modes of the electric field in an optical fiber can be transformed into an Optical-Schrödinger equation, where the z-axis of the optical fiber is analogous to time [36–39]. Hence, the classical electromagnetic wave equation can be used to mimic the quantum features and facilitate a proper experimental implementation. H. J. Stöckmann et al. had already explored this type of analogy between electromagnetic waves and quantum mechanics to explore quantum chaos using a two-dimensional microwave cavity [40–43]. Here, we use geometries inspired from the studies of quantum chaos to explore the geometric dependence of entanglement. In the recent decade, researchers had analyzed chaotic optical fibers for different purposes, V. Doya et al. had analyzed the speckle statistics and optical scars respectively in a D-shaped chaotic fiber [44, 45].

In this article, we introduce the idea of exploiting an optical fiber with a core cross-section that has the geometry of a chaotic billiard to create highly classically entangled light beams. More specifically, we analyze in this paper an optical fiber which possesses the cross sectional geometry of the Robnik billiard. By analyzing the propagation of a classical electromagnetic wave in these fibers, we can explore the geometric dependence of the classical entanglement in terms of the lowest-order eigenmodes, as well as using coherent and squeezed coherent states as the initial wavepackets.

2. Two-dimensional Optical-Schrödinger equation

It is well known that a light beam propagating in an optical fiber can be described by the following equation,

$$i\lambda_w \frac{\partial \psi(x,y,z)}{\partial z} = -\frac{\lambda_w^2}{2n_0(z)}\nabla_{xy}^2 \psi(x,y,z) + \frac{1}{2n_0(z)}[n_0^2(z) - n^2(x,y,z)]\psi(x,y,z), \quad (1)$$

which is a two-dimensional Optical-Schrödinger equation with an optical-wavefunction in the transverse x and y variables. The longitudinal coordinate z along the fiber axis is similar to time in the standard Schrödinger equation [36–39]. This type of analogy between quantum mechanics and wave optics has been also pointed out in many other works [46–48]. Here $n_0(z)$ is the refractive index along the beam axis and λ_w is the wavelength of the electromagnetic wave. Hence, the optical Hamiltonian can be written as,

$$H = \frac{1}{n_0(z)}\left(\frac{p_x^2}{2} + \frac{p_y^2}{2}\right) + U(x,y,z), \quad (2)$$

where p_x and p_y are the classical momentum variables in the transverse two-dimensional plane and the optical potential function has the form $U(x,y,z) = \frac{1}{2n_0(z)}[n_0^2(z) - n^2(x,y,z)]$. This type of two-dimensional Hamiltonian has already been studied in the context of chaotic ray propagation in an optical fiber [49]. In the usual sense, the classical limit corresponds to $\hbar \to 0$, while in the Optical-Schrödinger equation this limit corresponds to $\lambda_w \to 0$ which is just the classical ray optics approximation. By properly choosing the refractive index profile, we can define our potential function.

Let D be the domain of the fiber core cross-section in the two-dimensional xy plane. The optical fiber is a dielectric medium with refractive index $n(x,y,z)$. It is known that for a step-index fiber, $n(x,y,z) = n_0$ in the core with $(x,y) \in D \cup \partial D$ and $n(x,y,z) = n_1$ in the cladding if $(x,y) \in \bar{D}$. We assume that the outer region of the cladding is sufficiently large so that it can
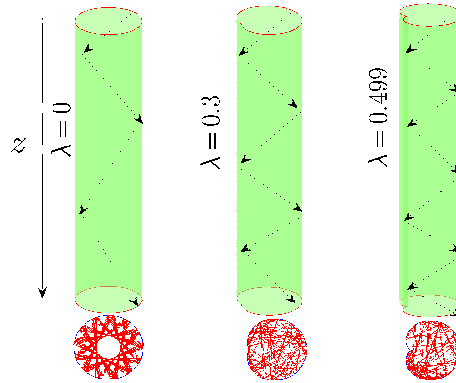
Fig. 1. This figure shows the geometry at the core of a family of the Robnik optical fiber. When $\lambda = 0$, the core of the optical fiber takes the standard circular shape. By increasing the deformation parameter λ, different quantum chaotic optical fibers are obtained. A schematic of the optical ray propagating in the z-direction is also shown as well as its projection on the xy plane which contains patterns reminiscent of a quantum chaotic billiard. Note that the z axis is the analog of time in the standard Schrödinger equation.

be taken to be infinite when considering guided light in the core and near the core-cladding boundary. Under this situation the components of the monochromatic electric and magnetic fields obey the Helmholtz equation [50]. In order to study the time evolution of the wavepacket, we define our two-dimensional potential as a function which is zero inside the domain (fiber core region) and relatively high outside the domain (cladding region). Hence our problem can be represented by the Helmholtz equation in a 2D domain which has been employed to describe diverse quantum chaotic billiards. In other words, our problem of the wavepacket propagation in an optical fiber has been reduced to a quantum chaotic billiard problem. The two-dimensional potential is taken as zero inside the domain and a high value of around 10^{12} outside the domain. This is enough to make the wavefunction to vanish on the outer boundary. In order to represent the two-dimensional potential on a grid, the Robnik billiard is represented in cartesian coordinates, which is given by,

$$((u+B)^2 + v^2 - 2B(u+B))^2 = A^2((u+B)^2 + v^2).$$

(3)

Using the cartesian form, the region inside and outside the Robnik billiard can be easily determined. Once the two-dimensional potential is obtained numerically, the wavefunction is propagated via the split operator method. Then, the density matrix is computed to evaluate the von Neumann entropy of entanglement S_{vn}.

In the classical limit, we study the dynamics of the classical billiard via ray optics while the wave optics description represents the analogous quantum mechanics in terms of the electromagnetic wave and its propagation in the waveguide. The quadrature components x, y, p_x and p_y are the position and momentum coordinate in the plane perpendicular to the fiber axis. This is clarified in Fig. 1 where we have shown the wave propagation in the optical fiber and its projection on the (x, y) plane. It is observed that the projection on the (x, y) plane is a chaotic Robnik billiard. Note that in our case x, y, p_x and p_y are exactly the coordinates and momentum variables of the chaotic Robnik billiard. In the ray optics limit, the path of light rays illustrate the chaotic properties while in the wave optics regime, the electromagnetic waves can exhibit

entanglement like features. The ray optics is analogous to classical mechanics and wave optics is analogous to quantum mechanics. Thus, the quantum-classical correspondence in quantum chaos is translated into wave optics - ray optics correspondence.

3. Mechanical modification of the classical entanglement

The goal of this article is to elucidate the effect of the domain boundary geometry on the classical entanglement. Our results would illustrate the possibility of manipulating classical entanglement via modifying the mechanical design of the core geometry. We shall entirely focus on the Robnik billiard due to its relative simplicity in terms of numerical computations. Our idea can be intuitively grasped from the following fact, that the eigenfunctions of a rectangular billiard are formed by a tensor product of x and y modes, and hence they are not entangled. By slightly deforming the rectangular geometry to a Bunimovich stadium, the eigenfunction would be changed entirely. The new eigenfunctions of the Bunimovich stadium then becomes a linear combination of the eigenfunctions of the rectangular billiard with proper boundary conditions and it is no longer a product state. The same is true for the Robnik billiard which results from deforming a circle. The eigenfunctions of the circular billiard [51] can be expressed as a tensor product state in terms of the r and θ variables as follows:

$$\phi_{m,n}(r,\theta) = J_m(j_{mn}r)e^{im\theta}. \tag{4}$$

In the radial direction, the eigenmodes are described by the Bessel functions $J_m(j_{mn}r)$, while the polar coordinates give the wavefunction $\Theta = e^{+im\theta}$ and j_{mn} describes the nth zero of the Bessel functions of order m. Hence, there is no entanglement between the polar and the radial part of the wavefunction for the circular geometry. By deforming the geometry, the classical entanglement starts to appear. For example, the eigenfunction of the Robnik billiard can be expanded in terms of the eigenfunctions of the circular billiard as follows:

$$\psi(\mathbf{r},\theta) = \sum_{m=0}^{N} \sqrt{C_m}J_m(\beta r)e^{im\theta}. \tag{5}$$

The value of β can be determined by minimizing the norm of the wavefunction on the boundary, which then gives the complete information about the wavefunction $\psi(\mathbf{r},\theta)$. This technique is often used in the numerical implementation of the method of particular solutions [52, 53]. Equation 5 shows that the wavefunction $\psi(\mathbf{r},\theta)$ is in the form of the Schmidt decomposition, where the Schmidt basis are the eigenfunctions of the circular billiard and the classical entanglement can be determined easily from the coefficients C_m. As the deformation increases, we need more terms to approximate the eigenfunction. Hence, the entanglement entropy would increase. When the beam paths configuration becomes highly chaotic, a larger number of Schmidt modes are required to approximate the eigenfunction which leads to a higher entanglement. This results from the fact that the field modes start to interact through the special geometry of the deformed circular boundary. This simple observation has far reaching consequences since it implies the possibility of manipulating classical entanglement via mechanical methods which is technically easy to achieve. In addition, chaos would serve to indicate the critical geometry that gives a maximum entanglement in the system.

In order to study the continuous variable entanglement of the transverse mode $\psi(\mathbf{r},\theta)$ in chaotic optical fibers, we first obtain the reduced density matrix of the first subsystem ρ_1 by integrating over the field variable θ in terms of the bipartite wavefunction $\psi(\mathbf{r},\theta)$ as follows:

$$\rho_1(\mathbf{r},\mathbf{r}') = \int \psi(\mathbf{r},\theta)\psi^*(\mathbf{r}',\theta)\sqrt{rr'}d\theta . \tag{6}$$
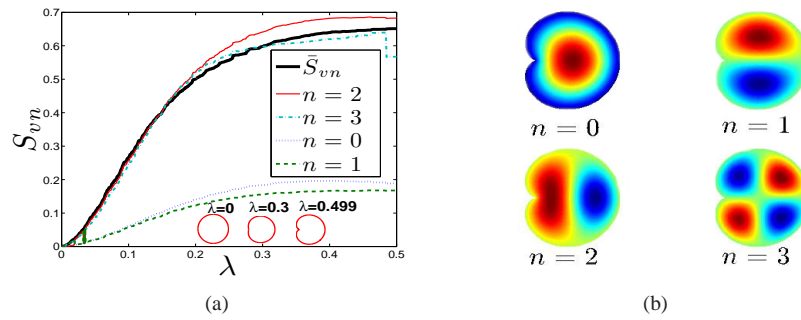
Fig. 2. The von Neumann entropy of entanglement S_{vn} of the four lowest eigenfunctions vs the deformation parameter λ of the Robnik fiber is shown in (a), while (b) shows the four lowest state eigenfunctions with $\lambda = 0.499$. It can be seen that the von Neumann entropy of entanglement S_{vn} in the eigenmodes saturates as the geometries of these fibers approach the completely chaotic regime. The solid black curve in (a) shows the average von Neumann entropy of entanglement of the ten lowest eigenmodes $\bar{S}_{vn}$ for different boundary geometries of the Robnik fiber.

To quantify the continuous variable classical entanglement, we compute the von Neumann entropy of the entanglement by using the numerical methods proposed by Parker et al. [54] and Bogdanov et al. [55]. The von Neumann entanglement entropy of the reduced density matrix is given by,

$$S_{vn}(t) = -\sum \eta_i \log \eta_i, \tag{7}$$

where η_i are the eigenvalues of the Hermitian kernel $\rho_1(\mathbf{r}, \mathbf{r}')$ as shown in Eq. 8 below. The eigenvalues are computed from the Fredholm type II integral equation of $\rho_1(\mathbf{r}, \mathbf{r}')$, which is given by

$$\int \rho_1(\mathbf{r}, \mathbf{r}')\phi_i(\mathbf{r}')dr' = \eta_i \, \phi_i(\mathbf{r}), \tag{8}$$

with $\phi_i(\mathbf{r})$ being the corresponding Schmidt eigenfunction.

4. Robnik fiber and classical entanglement

The cross section of a Robnik fiber has the shape of the Robnik billiard which is shown in Fig. 1. As light passes though the Robnik fiber the transverse modes of the fiber get entangled. We are interested in the optimum geometry which gives a high entanglement in the system. The cross sectional geometry of the Robnik fiber is a conformal transformation $w = AZ(\theta) + BZ(\theta)^2$ of the unit circle $Z(\theta)$ on the complex plane. According to Robnik [6], the cross-sectional geometry can be written in the parametric form as follows,

$$u = A\cos\theta + B\cos 2\theta \tag{9}$$
$$v = A\sin\theta + B\sin 2\theta. \tag{10}$$

The area of the billiard is given by $Area = \pi(A^2 + 2B^2)$ and by means of a reparametrisation, A and B can be written as follows: $A = \cos p$ and $B = \frac{1}{\sqrt{2}}\sin p$, where p is given by $p = \tan^{-1}(\lambda\sqrt{2})$. This allows us to define a family of closed analytical boundaries of constant area, $Area = \pi$, which depends on the values of the deformation parameter λ. Robnik had shown that the parameter λ can be chosen within the interval $0 \le p \le p_{sing} = \tan^{-1}\left(\frac{1}{\sqrt{2}}\right)$. For
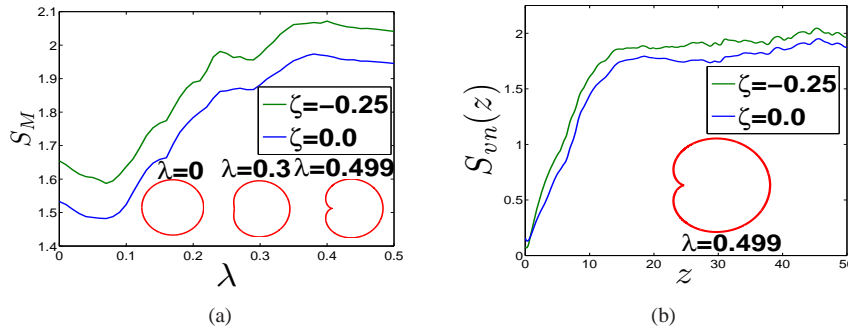
Fig. 3. A plot of the classical entanglement of the squeezed coherent state versus the deformation parameter λ of the Robnik fiber is shown in (a). We observe that the classical entanglement is higher when the system is in the chaotic regime and the initial squeezing has enhanced the classical entanglement in the system. In (b), we have plotted the classical entanglement dynamics as the light propagates along the z-axis. It is important to note that the light enters the fiber without any classical entanglement. Entanglement increases as it propagates, and as it traverses a distance of 50 units the classical entanglement saturates. Note that the blue and green curves represent the coherent state and the squeezed coherent state respectively. We have chosen the initial state at the point $(x, p_x, y, p_y) = (0.25, 0.1, 0.0, 0.1)$.

smaller values of λ, the billiard exhibits a regular dynamics since it is closer to the circular geometry. An increase in the parameter λ shifts the system from regular to chaotic. We analyze the dependence of the classical entanglement as we vary the deformation parameter λ from the regular to the chaotic regime.

4.1. Classically entangled Robnik eigenmodes

We have varied the fiber cross section by adjusting the deformation parameter λ. As the boundary geometry changes, we compute the lowest order eigenfunctions, so that the classical entanglement in the radial r and the angular θ modes can be evaluated. Based on our earlier discussion, the classical entanglement in the circular geometry between the r and θ variable is zero since the eigenfunction is a product state. As we change λ, the classical entanglement in the system starts to increase. In Fig. 2(a), we have plotted the classical entanglement of the eigenmodes against different values of the deformation parameter λ. In the same figure, we have also displayed the corresponding boundary geometry. We observe from Fig. 2(a) that the classical entanglement dynamics increases as λ increases. As the boundary geometry leads to chaotic behavior, the classical entanglement in eigenmodes increases even further and as the system approaches the highly chaotic regime the entanglement entropy saturates. Thus, the degree of chaos in the system is directly linked to the level of classical entanglement in the light pulse albeit there is a maximum attainable level in lieu of the eventual saturation. We have plotted the eigenmodes corresponding to the saturation level at $\lambda = 0.499$ in Fig. 2(b). From Fig. 2(a), we observe that the lowest energy mode $n = 0$ has higher classical entanglement compared to the excited mode $n = 1$. This can be understood by examining Fig. 2(b), where the ground state eigenmode is seen to be more severely affected by the deformation of the boundary, while the first excited mode $n = 1$ contains a nodal line through its center and has a form that is closer to the eigenmodes of the circular cross-section. Hence, the deformation in the eigenfunction is smaller for the $n = 1$ mode. The number of basis terms to describe this eigenfunction is smaller, which implies that its classical entanglement is smaller. The same argument applies to the ex-
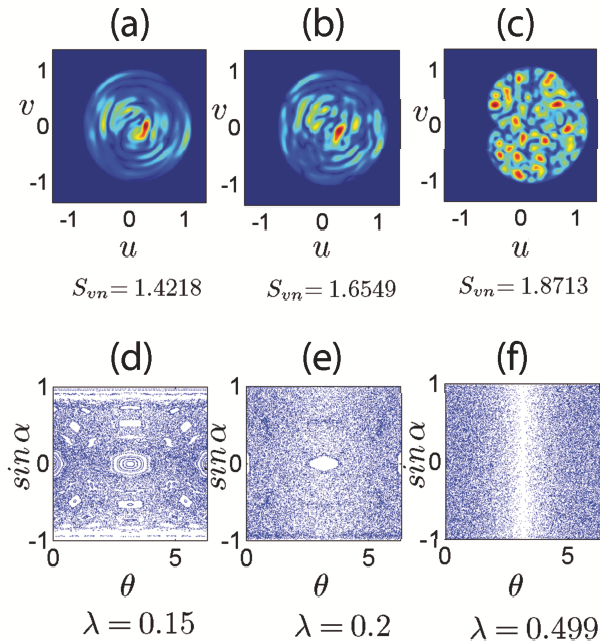
Fig. 4. The probability densities $|\psi(\mathbf{r}, \theta)|^2$ of the entangled coherent states coming out of the Robnik fiber with length $z = 50$ units are shown in (a), (b) and (c) with $\lambda = 0.15$, $\lambda = 0.2$ and $\lambda = 0.499$ respectively. The probability densities $|\psi(\mathbf{r}, \theta)|^2$ are shown in the cross-sectional $u - v$ plane of the fiber. The blue color shows the regions where the probability is zero and the red color shows the regions of higher probability. The entangled state is obtained from a tensor product coherent state centered at $(x, p_x, y, p_y) = (0.25, 0.1, 0.0, 0.1)$ with $\lambda_w = 0.01$. The entangled state occurs after the light beam has propagated a distance of $z = 50$ units. Note that we have also indicated the von Neumann entanglement entropy S_{vn} of the polar coordinates below these figures. In (d), (e) and (f) the corresponding classical phase space is shown for $\lambda = 0.15$, $\lambda = 0.2$ and $\lambda = 0.499$ respectively. From the figure it can be observed that the time evolved coherent state has a higher classical entanglement when the corresponding geometry possesses a larger degree of chaotic behavior.

cited modes $n = 2$ and $n = 3$, respectively. These results indicate that the eigenfunctions that are affected more by the boundary deformation would have a higher optical entanglement. It thus provides insights into how the chaotic geometry can be effectively used to produce highly classically entangled states.

4.2. Effect of squeezing and classical entanglement in the Robnik fiber

While it is typical to propagate a Gaussian beam in an optical fiber, one may wonder the effect of initially squeezing such a beam before launching it into the fiber. This question has led us to investigate the difference in classical entanglement dynamics with respect to the initial coherent and the squeezed coherent state as the light wave propagates in the horizontal z direction. For our investigation, we use the Hollenhorst and Caves definition of the squeezing operator [56–58] and we employ the coordinate representation of the squeezed coherent state [59] for the numerical computations. The squeezed coherent state is defined as

$$|\alpha_k, \zeta_k\rangle = \hat{D}(\alpha_k)\hat{S}(\zeta_k)|0\rangle, \tag{11}$$

where the displacement operator $\hat{D}$ and the squeezing operator $\hat{S}$ is given by

$$\hat{D}(\alpha_k) = \exp\left(\alpha_k \hat{a}_k^\dagger - \alpha_k^* \hat{a}_k\right), \tag{12}$$

$$\hat{S}(\zeta_k) = \exp\left(\frac{1}{2}\zeta_k \hat{a}_k^{\dagger 2} - \frac{1}{2}\zeta_k^* \hat{a}_k^2\right), \tag{13}$$

and $\alpha_k = |\alpha_k|e^{i\phi_k}$, $\zeta_k = |r_k|\, e^{i\theta_k}$ are complex numbers and α_k are related to the phase space variables (q_k, p_k) in the following manner

$$\alpha_k = \frac{1}{\sqrt{2\hbar}}(q_k + \mathrm{i}p_k), \tag{14}$$

with $k = 1, 2$, respectively. According to Møller et al. [59], the squeezed coherent state in the position basis can be written as

$$\psi(\mathbf{x}, \alpha_k, \zeta_k) = \left(\frac{1}{\pi\hbar}\right)^{1/4}(\cosh r_k + e^{i\theta}\sinh r_k)^{-1/2}$$
$$\exp\left\{-\frac{1}{2\hbar}\left(\frac{\cosh r_k - e^{i\theta}\sinh r_k}{\cosh r_k + e^{i\theta}\sinh r_k}\right)(\mathbf{x} - q_1)^2 + \frac{\mathrm{i}}{\hbar}p_1(\mathbf{x} - q_1/2)\right\}. \tag{15}$$

The tensor product state of this wavefunction is used to study the classical entanglement dynamics for different squeezing parameter values.

In Fig. 3(a) the classical entanglement maximum S_M is plotted against different fiber geometries. The classical entanglement maximum S_M is taken from the von Neumann entropy of entanglement $S_{vn}(z)$ which is computed for the propagation of the initial states along the z-axis with a fixed geometry. The initial tensor product coherent state and the squeezed coherent state is propagated for a different boundary geometry and we take these initial states to be centered at $(x, p_x, y, p_y) = (0.25, 0.1, 0.0, 0.1)$. We have computed the classical entanglement present in the radial and polar variables of the optical wavefunction. In Fig. 3(b) the classical entanglement dynamics of the coherent state and squeezed coherent state is plotted against the z-axis. When the optical wave with a tensor product coherent state enters the fiber (at $z = 0$), its classical entanglement is zero. During its propagation along the z-axis the transverse modes get entangled and after traveling a distance of 50 units along the z-axis, the classical entanglement becomes saturated. In other words, we observe that a non-entangled light enters at one end of the fiber and comes out entangled at the other end. In the case of a highly chaotic fiber with $\lambda = 0.5$,

this classical entanglement can yield a higher value. Note that we have chosen the initial condition $(x, p_x, y, p_y) = (0.25, 0.1, 0.0, 0.1)$ because it lies entirely inside the domain for the chosen parameter range of λ. The wavelength (analog of $\hbar$) given in Eq. 1 is selected as $\lambda_w = 0.01$. The value of λ_w is set small enough in order for the wavepacket to be contained entirely inside the defined two-dimensional cross-sectional domain. We have also used the equally position squeezed $\zeta_1 = \zeta_2 = \zeta$ wavepacket at a relatively small value of $\zeta = -0.25$ due to the numerical considerations. From Figs. 3(a) and 3(b) we can clearly see that as the core boundary deformation λ increases, the production of classical entanglement is found to increase for both the case of initial coherent state and initial squeezed coherent state. This is again observed in Figs. 4(a), 4(b) and 4(c) according to the corresponding von Neumann entropy of entanglement. It is well known that when the deformation parameter approaches $\lambda = 0.5$, the dynamical behavior of the classical system is highly chaotic (see Figs. 4(d), 4(e) and 4(f)) with the higher classical entanglement maxima observed in the corresponding optical system. Thus, our results clearly indicate the effect of the geometrical deformation on entanglement dynamics of initial squeezed coherent states in a chaotic optical fiber. It is to be noted that a judicious choice of a chaotic core cross-section would lead to the generation of highly entangled transverse modes. These results are also in accordance with our previous studies [4, 60].

Taking into account the recent experimental progress to quantify the classical entanglement [28], we do believe that an experiment can be performed as follows. After passing light beams through a chaotic optical fiber, the transverse field modes of light will get classically entangled. Changing the geometry of the fiber cross-section can affect the transverse mode intensity profile. The intensity measurement of the transverse electric field can be recorded on a CCD camera and this information can be used to measure the effect of geometry on the classical entanglement.

5. Conclusions

We have explored the dependence of the classical entanglement with the boundary deformation. We have seen that as the boundary gets deformed into a chaotic billiard, the entanglement in the eigenmode increases. This demonstrates that the classical entanglement has a dependence on the boundary geometry and the associated chaotic dynamics. We have also analyzed the propagation of a coherent state and a squeezed coherent state in a chaotic Robnik optical fiber. We have found that an initial squeezing can indeed enhance classical entanglement in chaotic optical fibers. More importantly, our results have specifically shown the cross-sectional geometry dependence of the classical entanglement.